Simulation of Carbonaceous Mesophases Micro-Textures

L.R.P. de Andrade Lima* and A.D. Rey**

Department of Chemical Engineering, McGill University
3610 University st., Montreal, Canada H3A 2B2
*ldeand@po-box.mcgill.ca, **alejandro.rey@mcgill.ca

ABSTRACT

Carbonaceous mesophases are liquid crystalline precursor materials that can be spun into high performance carbon fibers using the conventional melt spinning process. Carbon fiber property optimization requires a better understanding of the principles that control the structure development during the fiber formation processes and the rheological processing properties. This work presents the elastic and continuum theory of liquid crystals and simulations of structure formation for pressure-driven flow of carbonaceous liquid crystalline precursors used in the industrial carbon fiber spinning process. The results of these simulations capture the formation of characteristic fiber micro-textures and provide new knowledge on the role of viscous and elastic effects in the spinning process.

Keywords: texture, modeling, carbon fibers, mesophase pitch.

1 INTRODUCTION

Carbon fibers are advanced materials widely used in aerospace, chemical, electronic, sport, construction, and transportation industries due to their unique features such as low density, high thermal conductivity and shock resistance, low thermal expansion and high modulus. This material can be produced by carbonization of polyacrylonitrile, pyrolysis of cellulose, or vapor growth. Since 1977 a new technique of melt spinning natural and synthetic mesophases pitches has been introduced [1]. This carbon fiber family has ultra-high modulus and a very high thermal and electrical conductivity values.

The manufacture of pitch carbon fibers uses carbonaceous mesophases precursors in conjunction with the fiber melt spinning process. Carbonaceous mesophase are textured anisotropic viscoelastic liquid crystalline materials formed by disc-like aromatic molecules. This material exhibits orientational order and positional disorder and is a discotic nematic thermotropic liquid crystal [2].

The cross-sectional texture of mesophase fibers is just the spatial distribution of the director field: **n**=function (r,θ), where (r,θ) are the polar coordinates. A typical folded texture and its molecular organization are shown in Fig. 1. If we neglect the oriented core, the texture consists basically of a set of rings located at L, whose thickness T decreases towards the fiber rim. The mechanisms that lead to concentric ring textures needs to be elucidated for the eventual optimization and control of pitch based carbon fiber textures.

In this paper we focus on how the average molecular orientation **n** is affected by a steady capillary Poiseuille flow; we characterize the processing conditions that lead to the emergence of ring patterns in the fiber cross-section, and characterizes the pattern sensitivity for increasing pressure-drops.

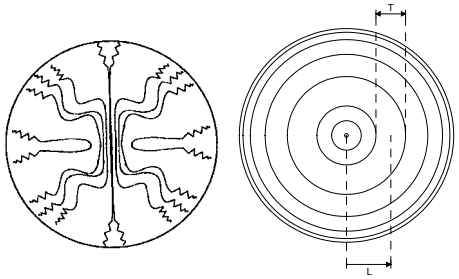

Figure 1: Microstructure of fiber cross-section: a) zig-zag pattern of folding becoming sharper and narrower toward the fiber edge [3], b) ring structure, with its thickness (T) and location (L).

2 GOVERNING EQUATIONS

The continuum theory of elasticity of liquid crystals takes into account external forces and torques that introduce deformations in the relative orientations and can distort the equilibrium configurations of liquid crystals [4,5]. The elastic free energy density F_d a nematic uniaxial liquid crystal material is given by:

$$F_d = \frac{K_{11}}{2}(\nabla \cdot \mathbf{n})^2 + \frac{K_{22}}{2}(\mathbf{n} \cdot \nabla \times \mathbf{n})^2 + \frac{K_{33}}{2}|\mathbf{n} \times \nabla \times \mathbf{n}|^2 \quad (1)$$

where the three basic modes of elastic storage are the splay (K_{11}), twist (K_{22}) and bend (K_{33}) modes.

The continuum theory of uniaxial nematic liquids consists of the linear momentum balance, director torque balance, and constitutive equations for the stresses, viscous and elastic torques that takes into account external forces distort the spatially uniform equilibrium configurations of liquid crystals [4,5]. For incompressible isothermal conditions the general conservation of linear and angular momentum are given by the follows equations:

$$\rho\left(\frac{\partial \mathbf{v}}{\partial t} + \mathbf{v} \cdot \nabla \mathbf{v}\right) = \mathbf{f} + \nabla \cdot \boldsymbol{\sigma} \quad (2)$$

$$\rho_1 \ddot{\mathbf{n}} = \mathbf{G} + \mathbf{g} + \nabla \cdot \boldsymbol{\pi} \quad (3)$$

where ρ is the density, **v** is the velocity vector, **f** is the body force per unit volume vector, **σ** is the total stress, ρ_1 is the moment of inertia per unit volume, **G** is the external director body force vector, **g** is the intrinsic director body force vector, and **π** is the director stress tensor.

Using transversely isotropic tensor coefficients, which reflect the material symmetry, the follow constitutive equations for the stress tensor and the director body force were proposed by Leslie [6]:

$$\boldsymbol{\sigma} = -p\mathbf{I} - \frac{\partial F_d}{\partial \nabla \mathbf{n}} \cdot \nabla \mathbf{n}^T \tag{4}$$
$$+ \alpha_1 (\mathbf{nn} : \mathbf{A})\mathbf{nn} + \alpha_2 \mathbf{nN} + \alpha_3 \mathbf{Nn} + \alpha_4 \mathbf{A} + \alpha_5 \mathbf{nn} \cdot \mathbf{A} + \alpha_6 \mathbf{A} \cdot \mathbf{nn}$$

$$\mathbf{g} = a\,\mathbf{n} - \boldsymbol{\beta} \cdot \nabla \mathbf{n} - \frac{\partial F_d}{\partial \mathbf{n}} - \gamma_1 \mathbf{N} - \gamma_2 \mathbf{n} \cdot \mathbf{A} \tag{5}$$

$$\boldsymbol{\pi} = \boldsymbol{\beta}\mathbf{n} + \frac{\partial F_d}{\partial \nabla \mathbf{n}} \tag{6}$$

where,

$$\mathbf{A} = (\nabla \mathbf{v} + \nabla \mathbf{v}^T)/2\,;\ \mathbf{W} = (\nabla \mathbf{v} - \nabla \mathbf{v}^T)/2\,;\ \mathbf{N} = \dot{\mathbf{n}} - \mathbf{W} \cdot \mathbf{n} \tag{7a,b,c}$$

$$\gamma_1 = \alpha_3 - \alpha_2\,;\ \gamma_2 = \alpha_6 - \alpha_5 = \alpha_3 + \alpha_2\,;\ \lambda = -\gamma_2/\gamma_1 \tag{8a,b,c}$$

$$\theta_s^k = k\pi + 1/2 \cos^{-1}(1/\lambda)\,,\quad k = 0, 1, 2, \ldots \tag{9}$$

p is the pressure, **I** is the unit tensor, $\{\alpha_i\}$, i=1…6, are the six Leslie viscosity coefficients that describes an anisotropic liquid, **A** is the rate of deformation tensor, **N** is the corotational derivative of the director vector, **β** is a Lagrange multiplier vector, γ_1 is the rotational viscosity, γ_2 is the irrotational torque coefficient, **W** is the vorticity tensor, λ is the reactive parameter, and θ^k_s are the k flow-alignment angles that exist when λ<-1. Note that $|\theta_s^{i+1}| = |\theta_s^i| + \pi$.

The Ericksen-Leslie theory predicts that for sufficiently large deformation rates, the director orients in the shear plane along the flow-alignment angle [4,5]. When the director field is homogeneous ($\nabla \mathbf{n} = 0$) and oriented at the alignment angle, the viscous and elastic torques vanish. Eq. (9) shows that the alignment angle is not unique. The primary alignement angle (n=0) defines the primary solution denoted by P_o, and secondary alignement angles (n>1) define secondary solutions denoted by S_n [7].

Assuming that the director orientation vector is confined to the (r,z) plane, as shows Fig. 1, $\mathbf{n}(r) = (\sin\theta(r), 0, \cos\theta(r))$, the director tilt angle (θ) in the steady state Poiseuille capillary flow of discotic nematic liquid crystals can be describe by the follows dimensionless equations [7,8] :

$$(\cos^2\theta + \varepsilon \sin^2\theta)\left(\frac{d^2\theta}{d\tilde{r}^2} + \frac{1}{\tilde{r}}\frac{d\theta}{d\tilde{r}}\right) + \frac{\sin 2\theta}{2}\left[(\varepsilon - 1)\left(\frac{d\theta}{d\tilde{r}}\right)^2 - \frac{1}{\tilde{r}^2}\right] - \frac{\tilde{H}(\theta)\,Er}{2\tilde{G}(\theta)}\tilde{r} = 0 \tag{10}$$

where ,

$$\tilde{G}(\theta) = \tilde{\alpha}_1 \sin^2\theta\cos^2\theta + \frac{(\tilde{\alpha}_5 - \tilde{\alpha}_2)}{2}\sin^2\theta + \frac{(\tilde{\alpha}_3 + \tilde{\alpha}_6)}{2}\cos^2\theta + \frac{\tilde{\alpha}_4}{2} \tag{11}$$

$$\tilde{H}(\theta) = \tilde{\alpha}_2 \sin^2\theta - \tilde{\alpha}_3 \cos^2\theta \tag{12}$$

$$Er = R^3(-dp/dz)/K_{11}\,; \qquad \varepsilon = K_{33}/K_{11} \tag{13a,b}$$

$$\tilde{\alpha}_i = \alpha_i/\bar{\eta}\,; \qquad \bar{\eta} = (\eta_1 + \eta_2 + \eta_3)/3 \tag{14c,d}$$

ε is the ratio of the bend and the splay Frank elastic constants, Er is the ratio of viscous flow effects to long-range elasticity effects, known as the Ericksen number, dp/dz is the pressure drop in the capillary per unit length, $\tilde{r}$ is the dimensionless radial distance ($\tilde{r} = r/R$), $\tilde{\alpha}_i$ are the dimensionless Leslie viscosity coefficients, $\bar{\eta}$ is the average Miesowicz' shear viscosity that describes an anisotropic liquid, and R is the capillary radius.

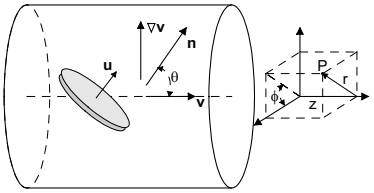

Figure 2: Capillary flow of uniaxial disc-like molecules with unit normal vector (**u**), director vector (**n**), velocity vector (**v**), velocity gradient (∇**v**), alignment angle (θ) between the director and the axial direction and the cylindrical (r,ϕ,z) coordinate.

The simulations were carried out using the parameters presented at Table 1, that correspond to the Frank elastic constants measured for hexakis(dodecanoyloxy)truxene and the six scaled Leslie coefficients calculated from non-equilibrium molecular dynamics simulations [9]; however, the results discussed in this paper are independent of the exact values of the viscoelastic parameters and arise whenever the reactive parameter (λ) is less than minus one. The orientation in the center of the capillary was assumed to be zero due to symmetry, and the anchoring angle at the wall, due to strong anchoring at the wall, was assumed to be zero.

The orientation equation, Eq.(10) was solved numerically using the Galerkin Finite Element method, and its integrals were computed using three-point Gaussian quadrature. The resulting set of non-linear equations was solved using the Newton-Raphson iteration scheme, and mesh independence was established using standard mesh refinement criteria.

Dimensionless Leslie viscosities coefficients (Eq. (14c))	
$\tilde{\alpha}_1$	0.000
$\tilde{\alpha}_2$	0.341
$\tilde{\alpha}_3$	1.765
$\tilde{\alpha}_4$	1.293
$\tilde{\alpha}_5$	-0.705
$\tilde{\alpha}_6$	1.402
Frank elastic constants (10^{-12} N)	
K_{11}	3.50
K_{33}	5.75

Table 1: Parametric Values [9]

3 RESULTS

The texture formation due to elastic effects fails to capture the length scales gradients are shown in real fibers [10]. This paper presents the texture formation model, which is driven by flow effects, and retains the elastic effects. As shown below the length scale distribution in the predicted flow-induced texture, in contrast to the elastic-induced texture, is consistent with experimental data, shown schematically in Fig. 1.

Figure 3 shows the director orientation (θ), obtained from Eq.10, as a function of dimensionless radial distance for Er=10000 for the primary (n=0) and five selected secondary (S_n, n=+4, +5, +9, +14, +16) solutions. It should be noted that the missing secondary solutions below the secondary solution $S_{+16,}$ not included in the plot, exist and are stable [7,8]. Figure 3 shows that higher order solutions exhibit a narrow alignment region in between core and rim regions over which the director vector exhibits also the same orientation periodically. On the other hand the low order solutions exhibit alignment over a wide annular region and narrow core and rim regions.

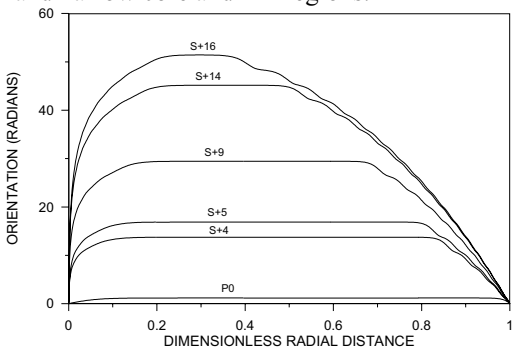

Figure 3: Director angle as a function of radial distance for the principal P_0 and five secondary solutions (S_k).

The solution multiplicity can help to explain micro-textural phenomena, such a multiple concentric ring formation, found in the flow processing of carbon mesophases. Figure 4 shows computed gray scale plots of the orientation profile shown in Fig. 3, for the n=16, 14, 9, 5, and 4 secondary solutions. The black color corresponds to the full alignment orientation ($\theta_s^k = \theta_s + k\pi$ radians, where k is an integer that gives the order of the secondary solution and θ_s is the first alignment angle, 1.157 in the present case) and the white color corresponds to the non-alignment orientation ($\theta = k\pi$ radians). The computed visualization of the orientation profiles give a ring texture with a characteristic ring thickness that is a function of position. The figures show that the number of rings is equal to the order of the solution. For example the n=4 solution has four rings, and so on. All the textures have three regions: a small core region surrounding the fiber axis, a large ring (black band) in the central annular region, and an outer rim region dense with thin rings. As n increases the width of the annular region decreases and the number of rings in the rim region increases.

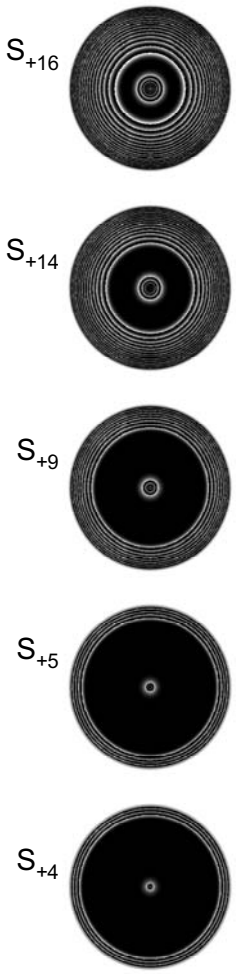

Figure 4: Texture simulation of the fiber cross section shown the average orientation to the secondary solutions (S_k) at Er=10000.

The previous discussion took into consideration the role of higher order solutions on the generation of the ring texture, now we consider the role of the pressure drop on the texture length scale T. Figure 5 shows the director angle (θ) as a function of the dimensionless radial distance for the secondary solution S+4, for Er=2728, 5000, 7500, and 10000. The figure shows that as Er increases the aligned annular region increases, and the rim region exhibits sharper and sharper gradients. The core region remains almost unaffected by pressure drop increases.

Figure 6 shows the corresponding computed visualizations, for the parametric conditions shown in Fig. 5. Again, in this plot, black corresponds to θ=1.157+kπ radians and white corresponds to θ=0+kπ radians. The figure shows that as Er increases, the number of rings remains constant, but they move towards the rim

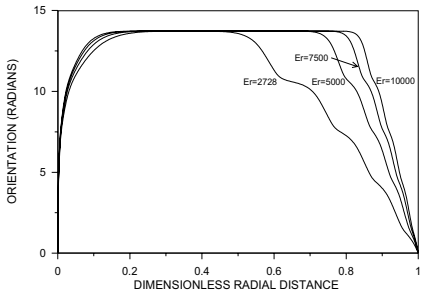

Figure 5: Director angle as a function of radial distance for secondary solution S_{+4} at Er=2728, 5000, 7500, and 10000

Figure 6: Texture simulation of the fiber cross section shown the average orientation to the secondary solution S_{+4} at Ericksen number 10000, 7500, 5000, and 2728.

Figure 7 shows the ring thickness (T) as a function of radial position (L), as defined in Fig. 1b, using the parametric conditions of Fig. 6. The picture shows that as Er increases T decreases, and the rings pile up at the rim. These predictions agree with the fact that as the higher shear rates close to the wall, it will refine the texture length scale T. The pressure drop has almost no effect at the core because at the center the shear rate vanishes and the structure remains unaffected by the flow. This result also shown that the pressure drop increases the location and thickness of the aligned annular region increases monotonically. Thus lower pressure drops produce more uniform textures than larger pressure drops. Since the number of rings remains constant, an increase in the annular region will result in compression of the rim region.

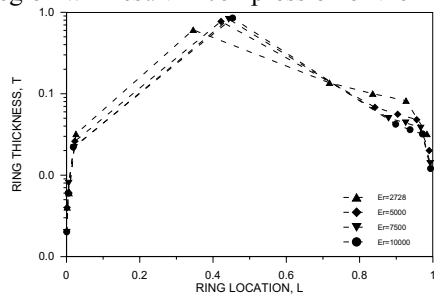

Figure 7: Rings thickness (T) versus ring location (L) to solution S_{+4}, and Er=2728, 5000, 7500, and 10000.

4 CONCLUSIONS

This work presentes the elastic and continuum theory of liquid crystals and simulations of structure formation for pressure-driven flow of carbonaceous liquid crystalline precursors. The results of these simulations capture the formation of characteristic fiber micro-textural phenomena, such as ring formation on carbon fiber textures of carbonaceous mesophases and provide new knowledge on the role of viscous and elastic effects in the carbon fiber spinning process.

ACKNOWLEDGMENT

This work was supported by the Engineering Research Centers Program of the NSF (EEC-9731680). LRPdAL also gratefully acknowledges NSERC (Canada) support.

REFERENCES

[1] D.D. Edie, In: Rand *et al* (Eds.), Design and Control of Structure of Advanced Carbon Materials for Enhanced Performance, Kluwer Academic Publishers, 163-181, 2001.
[2] A.D. Rey and M.M. Denn, Annual Reviews in Fluid Mechanics, 34, 233-266, 2002.
[3] G.M. Pennock, G.H. Taylor, J.D. FitzGerald, Carbon, 31(4), 591-603, 1993.
[4] F. R. S. Chandrasekhar, "Liquid Crystals", Cambridge University Press, 1992.
[5] P.G. de Gennes and J. Prost, "The Physics of Liquid Crystals", Oxford University Press, 1993.
[6] F.M. Leslie, Adv. Liq. Cryst., 4, 1-81, 1979.
[7] L.R.P. de Andrade Lima and A.D. Rey, Journal of Non-Newtonian Fluid Mechanics, 110(2-3), 103-142, 2003.
[8] L.R.P. de Andrade Lima and A.D. Rey, Materials Research, 6(2), 285-293, 2003.
[9] A.S.K. Ho and A.D. Rey, Rheological Acta, 30, 77-88, 1991.
[10] L. Wang and A.D. Rey, Liquid Crystals, 23, 93-111, 1997.